

Mean-Field Analysis of Amorphous Rare Earth-Transition Metal Alloys for Thermomagnetic Recording

MASUD MANSURIPUR AND M. F. RUANE

Abstract—A mean-field model is developed for amorphous ferromagnetic materials with potential applications in thermomagnetic recording/magneto-optical readout systems. The emphasis is on the reduction of the number of adjustable parameters, so that important variables and their effects on magnetic properties can be investigated. The available experimental data on GdCo-, GdFe-, and TbFe-based alloys is compared with the model predictions and good agreement is obtained in all cases. Expressions for the exchange stiffness coefficient and macroscopic anisotropy energy constant are derived and the latter is compared with available experimental data. The results have been used to study domain wall characteristics of the three material systems.

I. INTRODUCTION

AMORPHOUS rare earth-transition metal (RE-TM) alloys have proved extremely suitable for thermomagnetic recording and magneto-optical readout applications [1]–[6]. In thin film form, these media exhibit strong perpendicular anisotropy, which makes them particularly useful for polar Kerr or Faraday effect readout. Being ferromagnetic, they possess a compensation point temperature that can be brought to the vicinity of room temperature by proper choice of composition. This feature preserves the uniform magnetic alignment of the media by preventing the magnetization from breaking into oppositely oriented domains. Moreover, the high coercivity around the compensation point protects the recorded data from stray magnetic fields. The amorphous nature of the films eliminates a significant source of noise previously encountered in polycrystalline media [7]. Surface roughness and grain boundary noise are no longer limiting factors in the readout performance of the RE-TM alloys.

The first step in the study of thermomagnetic recording and erasure processes in the RE-TM alloys is the development of a model that can explain the behavior of magnetization versus temperature [8], [9]. Mean-field theory provides a simple solution to this problem, although its usefulness has been marred in the past by the existence of too many adjustable parameters [10]–[15]. Our goal in this paper is to develop a mean-field model for amorphous RE-TM alloys that can explain the available data with as

few adjustable parameters as possible. There is a fundamental difference between our model and the previous models for iron-based alloys, however. We have allowed for an antiferromagnetic iron subnetwork to account for the large variation of the Fe-Fe exchange interaction with interatomic distance. The possibility of antiferromagnetic interaction among iron atoms has been discussed in the literature [14], but, to our knowledge, has not been introduced into the mean-field models. The presence of both ferro- and antiferromagnetic Fe-Fe exchange gives rise to different magnetic moments for the iron subnetworks at nonzero temperatures. Further experimental evidence is thus called for in order to justify this assumption.

The organization of the paper is as follows: in Section II we define the parameters and derive the major equations of the mean-field theory. Section III is concerned with the explanation of the observed behavior of GdCo-, GdFe-, and TbFe-based alloys. In Section IV, the effect of uniaxial single-ion anisotropy on the mean-field model is discussed. Sections V and VI are devoted to the exchange stiffness coefficient and the macroscopic anisotropy energy constant, respectively. Section VII contains a few final remarks and a comparison of the three material systems in terms of their domain-wall properties.

II. MEAN-FIELD THEORY

We describe a mean-field model for an amorphous system with three magnetic subnetworks. Nonmagnetic elements are also included in this model insofar as they affect the densities and the coordination numbers of magnetic elements. The following notation is used throughout the paper:

N	total number of atoms (ions) in unit volume (cm^3)
x_n	atomic percentage of the n th species in the compound
r_n	atomic radius
Z_n	coordination number (average number of nearest neighbors)
S_n	spin angular momentum quantum number
L_n	orbital angular momentum quantum number
J_n	total angular momentum quantum number
g_n	gyromagnetic factor
J_{mn}	exchange integral between ions of species m and n

Manuscript received November 5, 1984; revised September 26, 1985. This work was supported by the National Science Foundation under Grant ECS-8307928 and in part by the IBM Corporation.

The authors are with Boston University, College of Engineering, 110 Cummington Street, Boston, MA 02215.

IEEE Log Number 8406521.

TABLE I
METALLIC RADII, ANGULAR MOMENTA, AND GYROMAGNETIC
FACTORS OF THE ELEMENTS USED IN THE MEAN-
FIELD CALCULATIONS.

	$r(\text{\AA})$	L	S	J	g
Gd	2.0	0	3.5	3.5	2.0
Tb	2.0	3.0	3.0	6.0	1.5
Co	1.4	0	adjustable		2.0
Fe	1.4	0	adjustable		2.0
Ar	2.0	—	—	—	—
B	1.2	—	—	—	—
Mo	1.5	—	—	—	—
Sn	2.0	—	—	—	—

The angular momenta for the rare earths are for the free ion states.

- M_n saturation magnetization of the n th subnetwork (emu/cc)
 M_s total saturation magnetization
 T absolute temperature ($^{\circ}\text{K}$)
 T_c Curie point temperature
 T_{co} compensation point temperature
 k Boltzmann's constant (1.38×10^{-16} ergs/ $^{\circ}\text{K}$)
 μ_B Bohr Magneton (9.27×10^{-21} ergs/G).

The subscript n refers to the n th subnetwork, and we will generally assume that $n = 1$ for the rare earth, $n = 2$ for the transition metal, $n = 3$ for the third magnetic element, and $n = 4, 5$ for nonmagnetic elements.

The atoms (ions) are assumed to be hard spheres and the radii r_n are calculated from a table of atomic concentrations [16] under the assumption that the atoms fill the entire space. The approximate values of r_n for materials of interest in this work are shown in Table I. Since amorphous materials are usually less dense than their crystalline counterparts, we assume that only 95 percent of the space is filled in the amorphous state [15]. The total number of atoms per unit volume N is thus given by

$$N = \frac{0.95}{\sum_{n=1}^5 (4\pi r_n^3/3) x_n} \quad (1)$$

The atomic density of the n th species is then equal to Nx_n .

The coordination numbers in amorphous materials are not constant and vary from site to site. For purposes of the mean-field theory, however, it suffices to have average values. Traditionally, researchers have assigned a fixed value, usually 12, to this parameter [10], [11]. We consider this inappropriate, particularly when the radii of the constituting elements differ significantly. In order to account for the dependence of Z_n on composition and atomic radii, the following approach is adopted here. Consider a sphere of radius r_n in contact with another sphere of radius r_m . Looking from the center of the first sphere, the spatial angle subtended by the second sphere is $4\pi \sin^2(\theta_{mn}/2)$ where $\theta_{mn} = \arcsin[r_m/(r_m + r_n)]$. The average number of atoms of species m that surround a given atom of species n is equal to $Z_n x_m$, and together they cover a fraction of space equal to $Z_n x_m \sin^2(\theta_{mn}/2)$ (as-

suming nonoverlapping cones). If we further assume that the entire space is filled by the nearest neighbor cones (an assumption which is only approximately valid in three dimensions), we obtain

$$\sum_{m=1}^5 Z_n x_m \sin^2(\theta_{mn}/2) = 1 \quad (2)$$

from which Z_n is readily calculated. In the special case in which all atoms are identical, Z_n turns out to be equal to 14.93, which is somewhat greater than the commonly used value of 12. However, since only relative values of Z_n are important in the mean-field model, this approximation should be acceptable.

The spin, orbital, and total angular momentum quantum numbers for the materials of interest are shown in Table I. The angular momenta of the rare-earth elements are identical with their free-ion values. This is a reasonable approximation considering the fact that the $4f$ electrons responsible for magnetic properties are well shielded by the $5s$ and $5p$ shells and are therefore largely unaffected by the environment. The values of S , L , and J for Tb and Gd are obtained by the Hund rules and are consistent with measured values [16].

The situation with transition metal elements is quite different. Here the magnetic electrons are in the $3d$ shell, whose structure is affected significantly by the local environment. The magnetic properties therefore vary with the composition and atomic structure of the alloy [17]. The orbital momentum is usually quenched in these materials, and thus the assumption of $L = 0$ is reasonable for our purposes. The $3d$ electrons occupy a band of energies split between electrons with up and down spins ($3d\uparrow$ and $3d\downarrow$ bands). The difference between the population of these bands determines the spin of the TM ion. The spin can thus assume noninteger values. Moreover, the band structure and the number of electrons available to each band vary with composition. The TM spin is thus a complicated function of the composition and structure of the alloy and, to simplify matters, we have used it as an adjustable parameter in our calculations.

The band structure of cobalt is believed to be of the form shown in Fig. 1(a) with the Fermi level above the $3d\uparrow$ band [17]. Assuming that alloying does not modify the band structure, addition of electrons can only fill the $3d\downarrow$ band and thereby reduce the net spin of individual cobalt ions. For iron, the structure is believed to be of the form shown in Fig. 1(b); here the Fermi level is within the $3d\uparrow$ band and, depending on the exact structure of the bands, addition of electrons could result in either an increase or a decrease of the net spin [17]. The band structure can be used as a guide in adjusting the numerical value of the spin, although, in the absence of more elaborate information, its usefulness is quite limited.

The gyromagnetic factor g is a proportionality constant that relates the magnetic moment and the total angular momentum. For pure orbital momenta $g = 1$, while for pure spin $g = 2$. In general, the value of g is obtained from the Lande equation [16].

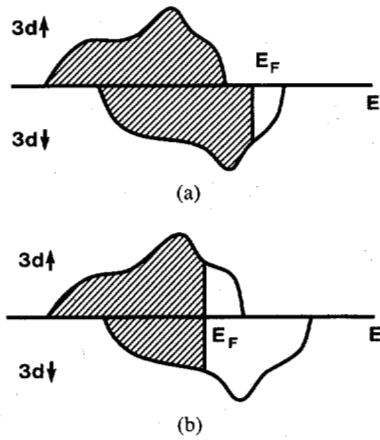


Fig. 1. 3d electronic band structure of the TM subnetwork.

The exchange integral is a quantum mechanical entity which arises from the overlap of electronic charge distributions. While in dielectric media the exchange interaction between neighboring atoms (ions) is direct, the interaction in metals is primarily mediated by the conduction electrons [17]. The magnitude and sign of \mathcal{J} are, in general, functions of the electronic structure of the ions and the distance between them. For a pair of ions with angular momenta J_m and J_n , the mutual energy in the classical approximation is given by

$$e_{mn} = -2\mathcal{J}_{mn}j_mj_n$$

where j_m and j_n are the projections of angular momenta along the axis of anisotropy. In the mean-field approximation the exchange energy of ion m resulting from its interaction with ion n is

$$e_m = -\mathcal{J}_{mn}j_m\langle j_n \rangle$$

where $\langle j_n \rangle$ is the time average of j_n . The total exchange energy of m arising from interactions with its nearest neighbors in our triple-magnetic-subnetwork model is thus given by

$$E_m = -Z_m j_m \sum_{n=1}^3 x_n \mathcal{J}_{mn} \langle j_n \rangle.$$

Since j_m can only assume the values of $-J_m, -J_m + 1, \dots, J_m - 1, J_m$, then

$$\langle j_m \rangle = \frac{\sum_{j_m=-J_m}^{J_m} j_m e^{-E_m/kT}}{\sum_{j_m=-J_m}^{J_m} e^{-E_m/kT}},$$

or, equivalently

$$\langle j_m \rangle = \left(J_m + \frac{1}{2} \right) \coth \left[\frac{Z_m (2J_m + 1) \sum_{n=1}^3 x_n \mathcal{J}_{mn} \langle j_n \rangle}{2kT} \right] - \frac{1}{2} \coth \left[\frac{Z_m \sum_{n=1}^3 x_n \mathcal{J}_{mn} \langle j_n \rangle}{2kT} \right]. \quad (3)$$

The three equations thus obtained with $m = 1, 2,$ and 3 must be solved simultaneously for the $\langle j_n \rangle$ at any given temperature. A numerical method which starts with reasonable initial values and iterates until a consistent solution is obtained was found to converge quickly and yield reliable solutions. The subnetwork magnetizations are then obtained from the relation

$$M_n = N x_n \mu_B g_n \langle j_n \rangle. \quad (4)$$

The Curie temperature T_c can be found analytically if we realize that around T_c the $\langle j_n \rangle$ values are small and if we use the approximation

$$\coth(x) = (1/x) + (x/3)$$

which is valid for $|x| \ll 1$. Thus, in the vicinity of T_c ,

$$\langle j_m \rangle = \frac{Z_m J_m (J_m + 1) \sum_{n=1}^3 x_n \mathcal{J}_{mn} \langle j_n \rangle}{3kT},$$

which, in matrix notation, is equivalent to

$$\begin{bmatrix} a_{11} & a_{12} & a_{13} \\ a_{21} & a_{22} & a_{23} \\ a_{31} & a_{32} & a_{33} \end{bmatrix} \cdot \begin{bmatrix} \langle j_1 \rangle \\ \langle j_2 \rangle \\ \langle j_3 \rangle \end{bmatrix} = T \begin{bmatrix} \langle j_1 \rangle \\ \langle j_2 \rangle \\ \langle j_3 \rangle \end{bmatrix}. \quad (5)$$

Here $a_{mn} = Z_m x_n \mathcal{J}_{mn} J_m (J_m + 1) / 3k$. Hence, the Curie temperature T_c must be an eigenvalue of the matrix $[a_{mn}]$. (It turns out that T_c is always the largest real eigenvalue.) This method allows the calculation of T_c without solving the mean-field equations for the entire range of temperatures.

III. COMPARISON OF MODEL CALCULATIONS WITH THE OBSERVED DATA

The mean-field theory of the last section has been employed to explain the experimentally observed behavior of saturation magnetization versus temperature in several RE-TM-based alloys. Instead of trying to obtain a close match in every case by varying all the adjustable parameters, we have tried to obtain a reasonable match with as few adjustable parameters as possible. This, we hope, will bring out the dominant trends and exclude the less significant factors.

We have studied three classes of materials for which experimental data has been available in the published literature. These are the classes of GdCo-, GdFe-, and TbFe-based alloys. For each class we have used a fixed set of exchange integrals \mathcal{J}_{mn} as shown in Table II. It is true that the local environment and the interatomic distances play a role in determining the values of the exchange integrals, and it is also true that by changing the composition in a given system of materials, these factors are more likely than not to change. We believe, however, that because of the nature of exchange in metallic alloys, the variation of exchange parameters is of secondary importance. An exception is made for $\mathcal{J}_{\text{Fe-Fe}}$, which is apparently very sensitive to the interatomic distance. In fact,

TABLE II
EXCHANGE INTEGRALS USED IN THE MEAN-FIELD CALCULATIONS

Material System	J_{TM-TM}	J_{RE-TM}	J_{RE-RE}
GdCo	28.0×10^{-15}	-2.2×10^{-15}	0.5×10^{-15}
GdFe	$\pm 12.0 \times 10^{-15}$ *	-1.7×10^{-15}	0.5×10^{-15}
TbFe	$\pm 8.5 \times 10^{-15}$ *	-1.0×10^{-15}	0.2×10^{-15}

*The minus sign applies to the antiferromagnetic subnetwork.

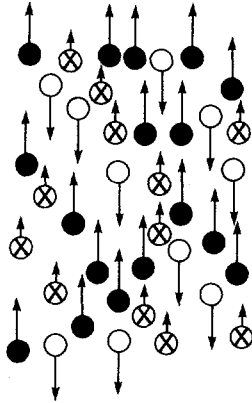


Fig. 2. A typical arrangement of moments in an RE-Fe alloy. The \circ is the rare earth, \bullet is the iron in the ferromagnetic subnetwork, and \otimes is the iron in the antiferromagnetic subnetwork. The net exchange field on each atom is the sum of contributions from its nearest neighbors. The contribution of \bullet and \circ to their iron neighbors, whether \bullet or \otimes , is always positive. The contribution of \otimes to a neighboring \bullet is positive, while its contribution to a neighboring \otimes is negative. If the fraction of \otimes in the alloy is not too large, then the net field on both \bullet and \otimes will be positive, while the net field on \circ will be negative. This is why both iron subnetworks have positive moments.

in certain compounds, the Fe-Fe exchange is known to be ferromagnetic for some iron pairs and antiferromagnetic for others [13]. Thus for the RE-Fe alloys, we have postulated the existence of two iron subnetworks: one with positive and another with negative Fe-Fe exchange ($\pm J_{Fe-Fe}$). The coupling between the two subnetworks, however, remains ferromagnetic ($+J_{Fe-Fe}$), and both subnetworks couple antiferromagnetically to the RE subnetwork with the same exchange parameter J_{RE-Fe} . The only new parameter thus introduced is the fraction α of iron in the antiferromagnetic subnetwork; α has been used as an adjustable parameter in our calculations. As long as α is not too large, the mean field on the antiferromagnetic subnetwork will remain parallel to, but smaller than, the field on the ferromagnetic subnetwork. The two kinds of iron will thus have parallel moments at all temperatures, but the moment of the antiferromagnetic kind will quickly decay with temperature. This means that at nonzero temperatures, the ferromagnetic iron atoms will have a larger moment than the antiferromagnetic ones. Fig. 2 shows a typical arrangement of moments at $T \neq 0$. At $T = 0$, the arrangement is the same but the two iron subnetworks have equal moments.

In Tables III-V, we have compared the experimental data collected from the literature with our model calculations. Information regarding the source of data, sample composition, preparation conditions, and measurement

methods is also given. In fitting the data we assumed that the nominal compositions are subject to a few percentage points of error, and thus searched the vicinity of the nominal composition for a good match. The best match usually was found within $\pm 1\%$ of the nominal. We also assumed the presence of a small amount of argon in the compounds to account for the impurities that are inevitably present in any sample. Since the measurement of magnetization requires a precise knowledge of the sample thickness, systematic errors are introduced if there is inaccuracy in the thickness measurement. Lack of instrument calibration is another source of systematic errors. In a few cases we had to allow for the possibility of such systematic errors in the data. Figs. 3-8 show some typical fits of the theoretical curves to the data.

Table III corresponds to GdCo-based alloys. A double-magnetic-subnetwork model has been sufficient for explaining the data. The cobalt moment J_{Co} is seen in all cases to be below the value of 0.86 for pure cobalt. This is consistent with the band model in which the $3d\downarrow$ band is successively filled with additional electrons. If we assume that Gd, B, and Mo atoms contribute 1.5, 2.5, and 3 electrons, respectively, to the d band, the values of J_{Co} obtained in these calculations can be explained. We emphasize, however, that charge transfer arguments are not completely reliable, and although we use them as guidelines in estimating the TM moment, we shall not rely heavily on the quantitative results.

Table IV corresponds to the GdFe-based alloys. A triple-magnetic-subnetwork model has been used to account for the antiferromagnetic coupling among a certain fraction of iron moments. The adjustable parameters are J_{Fe} and the fraction α of iron in the antiferromagnetic subnetwork. It can be seen that, with addition of Gd, the iron moment decreases from 1.11 for pure iron to a minimum of 0.95 at around 25 percent Gd. Adding more gadolinium seems to increase the moment again. The fraction of antiferromagnetic iron, α , varies between 0.3 and 0.5 for pure GdFe alloys. This may represent the effect of the deposition environment on the structural characteristics of the alloy. In the three compounds containing Sn or B, the antiferromagnetic subnetwork is absent and the iron moment remains around 0.95. The absence of antiferromagnetic iron here may be a result of the reduced iron concentration in the alloy, but it is difficult to arrive at any conclusions at this point without further experimental evidence.

Table V corresponds to the TbFe-based alloys. Again, the adjustable parameters are J_{Fe} and α . With the addition of Tb, the iron moment seems to decrease to a minimum of 0.96 around 19 percent Tb, and then rises again. The similarity of this behavior for GdFe and TbFe is encouraging, and may in fact suggest that a band structure such as shown in Fig. 9 is at work.

To appreciate the significance of the antiferromagnetic iron subnetwork in these calculations, we have plotted in Fig. 10 the Curie and compensation point temperatures versus α for a typical alloy. It is observed that the Curie

TABLE III
COMPARISON BETWEEN THEORETICAL AND EXPERIMENTAL DATA ON GdCo-BASED ALLOYS

	Nominal Composition	Ref.	Deposition Method	Composition Analysis Method	Magnetization Measurement Method	Theoretical (Best Match) Composition	J_{Co}
1	Gd _{21.5} Co _{78.5}	[1]	sputtering	XRF	Force-Balance	(Gd _{22.5} Co _{77.5}) ₉₅ Ar ₅	0.63
2	Gd _{22.1} Co _{77.9}	[15]	e-beam evaporation	microprobe	VSM	(Gd _{21.5} Co _{78.5}) ₉₅ Ar ₅ *	0.63
3	Gd ₁₈ Co ₇₅ B ₆ Ar ₁	[13]	sputtering	microprobe	Force-Balance	Gd _{15.5} Co _{77.5} B ₆ Ar ₁	0.53
4	Gd ₇ Co ₇₄ Mo ₁₃ Ar ₆	[19]	sputtering	—	—	Gd ₈ Co ₇₅ Mo ₁₂ Ar ₅	0.53
5	Gd ₁₅ Co ₇₄ Mo ₁₁	[21]	sputtering	—	—	(Gd ₁₅ Co ₇₄ Mo ₁₁) ₉₄ Ar ₆	0.49
6	Gd ₁₁ Co ₅₉ B ₁₃ Ar ₁₇	[13]	sputtering	microprobe	Force-Balance	Gd ₁₁ Co ₅₉ B ₁₃ Ar ₁₇	0.45
7	(Gd ₁₀ Co ₇₃ Mo ₁₇) ₉₈ Ar ₂	[12]	sputtering	microprobe	VSM	(Gd _{10.5} Co _{72.5} Mo ₁₇) ₉₅ Ar ₅	0.40
8	Gd _{11.3} Co _{67.2} Mo ₁₆ Ar _{5.5}	[19]	sputtering	—	—	Gd _{12.5} Co _{66.5} Mo ₁₆ Ar ₅	0.39

* Argon is used here to represent impurities in the sample. The effect of nonmagnetic impurities is only on the density and coordination numbers, and in that respect argon can be substituted for other contaminants. In reality, sputtered films contain a certain amount of argon while evaporated films are likely to be contaminated by other elements.

TABLE IV
COMPARISON BETWEEN THEORETICAL AND EXPERIMENTAL DATA ON GdFe-BASED ALLOYS

	Nominal Composition	Ref.	Deposition Method	Composition Analysis Method	Magnetization Measurement Method	Theoretical (Best Match) Composition	J_{Fe}	α
1	Gd ₁₉ Fe ₆₇ B ₁₂ Ar ₂	[13]	sputtering	microprobe	VSM	Gd ₁₉ Fe ₆₆ B ₁₂ Ar ₃	0.92	0
2	Gd ₂₀ Fe ₆₀ B ₁₈ Ar ₂	[13]	sputtering	microprobe	VSM	Gd ₂₀ Fe ₆₀ B ₁₈ Ar ₂	0.95	0.
3	Gd _{24.5} Fe _{69.5} Sn ₆	[6]	e-beam evaporation	microprobe	VSM	(Gd _{23.5} Fe _{70.5} Sn ₆) ₉₀ Ar ₁₀	0.95	0.
4	Gd ₂₆ Fe ₇₄	[6]	e-beam evaporation	microprobe	VSM	(Gd ₂₅ Fe ₇₅) ₉₅ Ar ₅	0.95	0.33
5	Gd ₂₄ Fe ₇₆	[2]	sputtering	XRF	VSM	(Gd ₂₅ Fe ₇₅) ₉₅ Ar ₅	0.95	0.4
6	Gd _{26.3} Fe _{73.7}	[15]	e-beam evaporation	microprobe	VSM	(Gd _{25.5} Fe _{74.5}) ₉₅ Ar ₅	0.96	0.33
7	Gd ₂₃ Fe ₇₇	[2]	sputtering	XRF	VSM	(Gd _{23.5} Fe _{76.5}) ₉₅ Ar ₅	0.97	0.4
8	Gd _{24.9} Fe _{75.1}	[15]	e-beam evaporation	microprobe	VSM	(Gd _{23.5} Fe _{76.5}) ₉₅ Ar ₅	0.97	0.33
9	Gd _{30.6} Fe _{69.4}	[15]	e-beam evaporation	microprobe	VSM	(Gd _{31.5} Fe _{68.5}) ₉₅ Ar ₅	1.12	0.48

TABLE V
COMPARISON BETWEEN THEORETICAL AND EXPERIMENTAL DATA ON TbFe-BASED ALLOYS

	Nominal Composition	Ref.	Deposition Method	Composition Analysis Method	Magnetization Measurement Method	Theoretical (Best Match) Composition	J_{Fe}	α
1	Tb ₁₄ Fe ₈₆	[22]	sputtering	—	—	(Tb ₁₃ Fe ₈₇) ₉₅ Ar ₅	1.02	0.5
2	Tb ₁₉ Fe ₈₁	[2]	sputtering	XRF	VSM	(Tb ₁₉ Fe ₈₁) ₉₅ Ar ₅	0.96	0.31
3	Tb ₂₁ Fe ₇₉	[2]	sputtering	XRF	VSM	(Tb _{20.5} Fe _{79.5}) ₉₅ Ar ₅	0.97	0.25
4	Tb ₂₂ Fe ₇₈	[22]	sputtering	—	—	(Tb _{21.5} Fe _{78.5}) ₉₅ Ar ₅	0.97	0.24
5	Tb ₂₉ Fe ₇₁	[22]	sputtering	—	—	(Tb ₂₉ Fe ₇₁) ₉₅ Ar ₅	1.14	0.3
6	Tb _{33.3} Fe _{66.7}	[23]	sputtering	—	—	(Tb ₃₄ Fe ₆₆) ₉₅ Ar ₅	1.10	0.35

temperature drops and the compensation point rises with increasing α . The reason is that the net exchange field acting on the antiferromagnetic iron subnetwork is small, and consequently the magnetization of this subnetwork decays rather quickly with temperature. The α value is thus an important parameter of our model because it allows the data to be explained with a fixed set of exchange parameters.

IV. SINGLE-ION ANISOTROPY AND THE MEAN-FIELD MODEL

In order to study the effect of single-ion anisotropy on the mean-field model, we have assumed that the rare earth

element is subject to uniaxial anisotropy of the simplest kind, and that its total energy is given by

$$E_1 = -Z_1 j_1 \sum_{n=1}^3 x_n \mathcal{J}_{1n} \langle j_n \rangle - D j_1^2. \quad (6)$$

Here D is the anisotropy constant with the axis of anisotropy perpendicular to the film plane. It follows that

$$\langle j_1 \rangle = \frac{\sum_{j_1=-J_1}^{J_1} j_1 e^{-E_1/kT}}{\sum_{j_1=-J_1}^{J_1} e^{-E_1/kT}}, \quad (7)$$

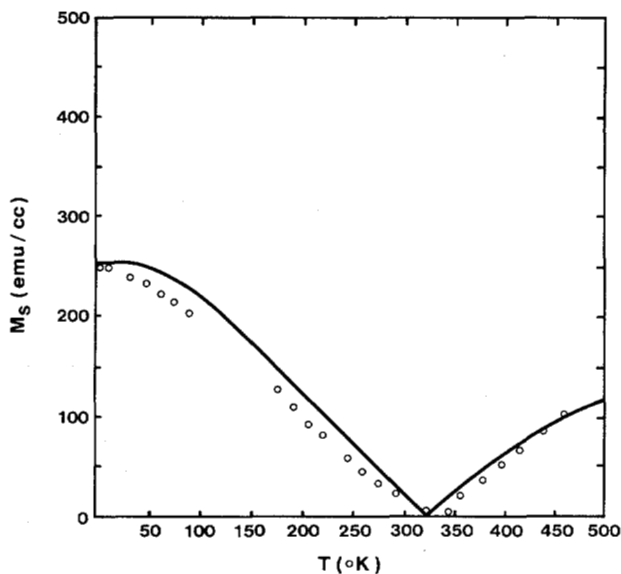


Fig. 3. Experimental (\circ) and theoretical (—) values of magnetization versus temperature for $\text{Gd}_{22.1}\text{Co}_{77.9}$ (reported composition). See row 2 in Table III.

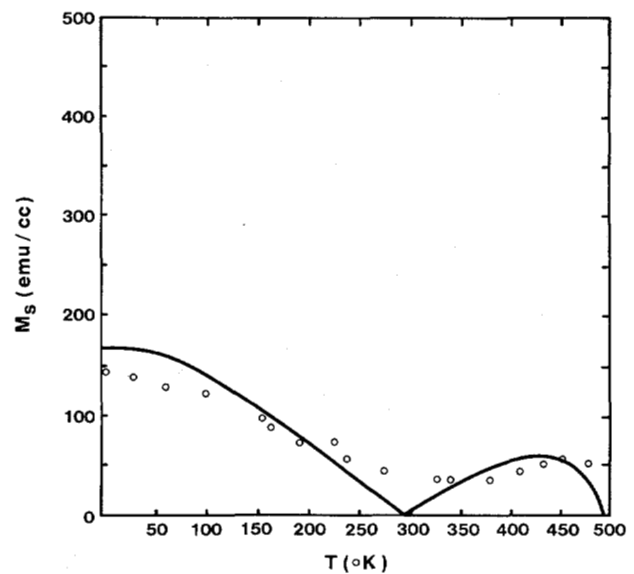


Fig. 5. Experimental (\circ) and theoretical (—) values of magnetization versus temperature for $\text{Gd}_{26.3}\text{Fe}_{73.7}$ (reported composition). See row 6 in Table IV.

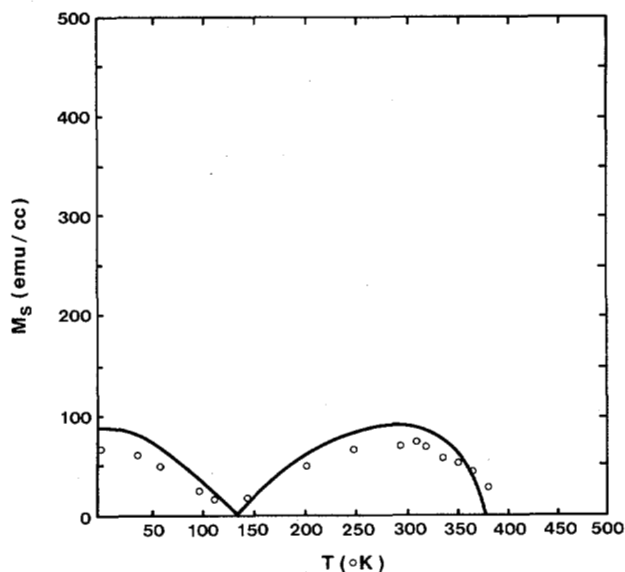


Fig. 4. Experimental (\circ) and theoretical (—) values of magnetization versus temperature for $(\text{Gd}_{10}\text{Co}_{73}\text{Mo}_{17})_{98}\text{Ar}_2$ (reported composition). See row 7 in Table III.

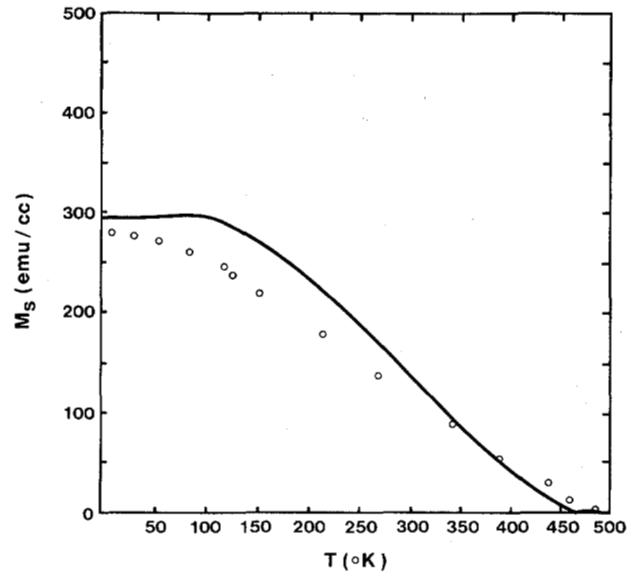


Fig. 6. Experimental (\circ) and theoretical (—) values of magnetization versus temperature for $\text{Gd}_{30.6}\text{Fe}_{69.4}$ (reported composition). See row 9 in Table IV.

while $\langle j_2 \rangle$ and $\langle j_3 \rangle$ are still given by (3). Although a closed form no longer exists for (7), the mean-field equations are still amenable to numerical solutions as before. Fig. 11 shows T_c and T_{co} versus D for a typical alloy. It is seen that the increase of T_c with D is rather insignificant, but the effect of D on T_{co} is dramatic.

In gadolinium-based alloys the single ion anisotropy is believed to be negligible. This is due to the fact that Gd is an S-state ion with little or no interaction with the "crystal" electric field. Terbium, on the other hand, is known to couple strongly to the electric field and create large amounts of single-ion anisotropy. It is thus expected that the best model for TbFe is one that includes both the single ion anisotropy of Tb and the antiferromagnetic coupling of Fe ions. However, as will be seen in Section VI,

the measured values of the macroscopic anisotropy energy constant seem to indicate that $D \sim 10^{-17}$ ergs, which is too small to affect our mean-field model calculations. It has been argued that the effective value of D is, in fact, much larger than the value suggested by the macroscopic measurements [18]. We feel, however, that a meaningful discussion of this subject is not possible until more reliable data is available.

V. EXCHANGE STIFFNESS COEFFICIENT

In the Heisenberg model the exchange energy density is given by [12]

$$E = -\sum_m \sum_n J_{mn} \langle \vec{j}_m \rangle \langle \vec{j}_n \rangle \quad (8)$$

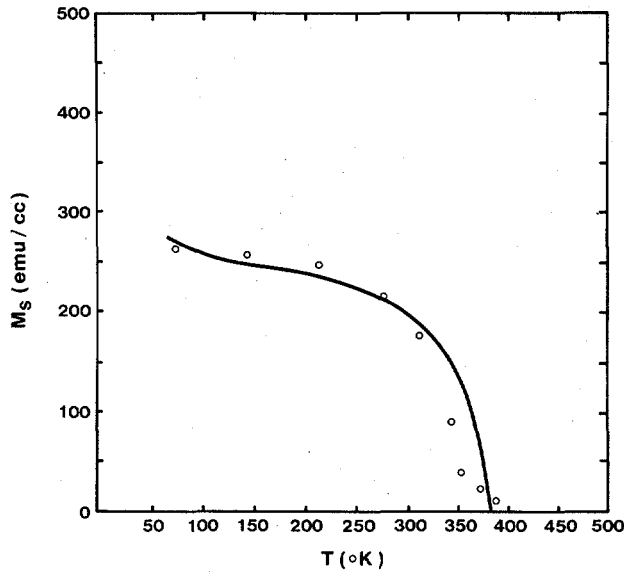


Fig. 7. Experimental (O) and theoretical (—) values of magnetization versus temperature for $Tb_{14}Fe_{86}$ (reported composition). See row 1 in Table V.

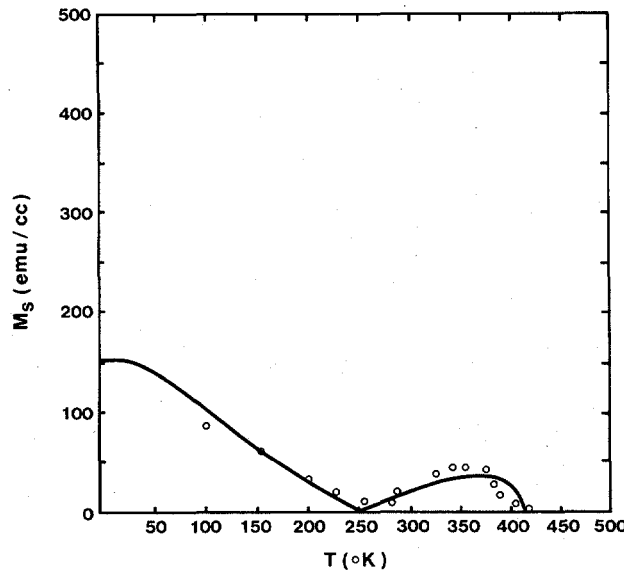


Fig. 8. Experimental (O) and theoretical (—) values of magnetization versus temperature for $Tb_{21}Fe_{79}$ (reported composition). See row 3 in Table V.

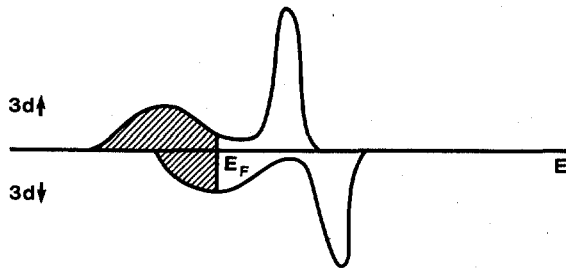


Fig. 9. A possible band structure for iron.

where the summations are over all sites in a unit volume and the assumption $\langle \vec{j}_m \vec{j}_n \rangle = \langle \vec{j}_m \rangle \langle \vec{j}_n \rangle$ is implicit. When we ignore all but nearest neighbor interactions, (8)

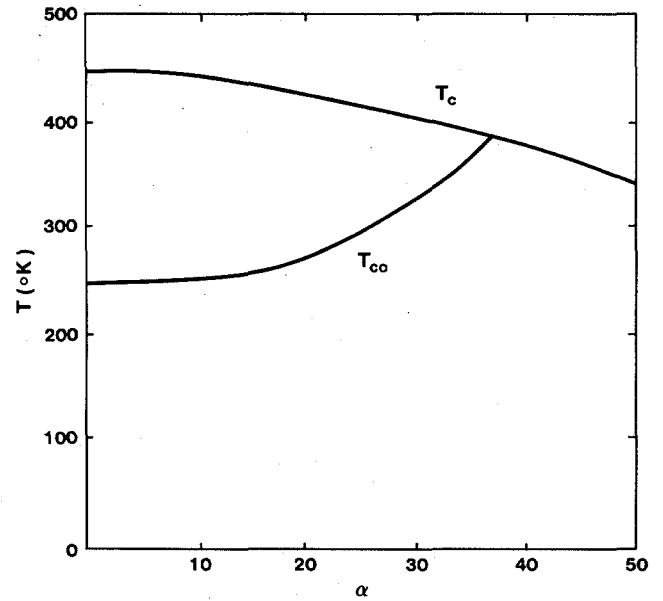


Fig. 10. Calculated Curie and compensation point temperatures versus α for $(Tb_{21}Fe_{79})_{95}Ar_5$ with $J_{Fe} = 0.97$.

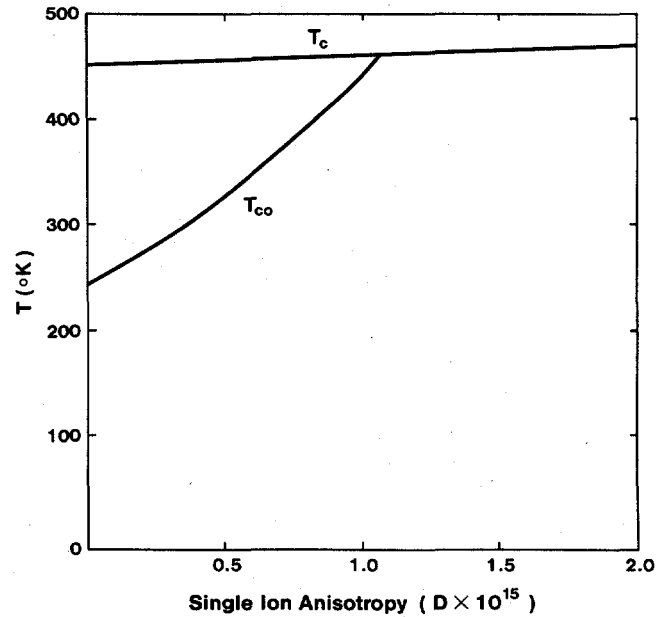


Fig. 11. Calculated Curie and compensation point temperatures versus single-ion anisotropy constant D for $(Tb_{21}Fe_{79})_{95}Ar_5$ with $J_{Fe} = 0.97$ and $\alpha = 0$.

becomes

$$E = -\sum_m \sum_n J_{mn} \langle j_m \rangle \langle j_n \rangle \cos(\theta_{mn}) \quad (9)$$

where m, n are nearest neighbors and θ_{mn} is the angle between $\langle \vec{j}_m \rangle$ and $\langle \vec{j}_n \rangle$. Now $\cos(\theta_{mn})$ must be replaced with its average over all orientations of m, n pairs. Let \vec{d} be the distance between a pair of unit vectors located at $\pm \vec{d}/2$ with direction cosines $(\alpha \pm \vec{\nabla}\alpha \cdot \vec{d}/2, \beta \pm \vec{\nabla}\beta \cdot \vec{d}/2, \gamma \pm \vec{\nabla}\gamma \cdot \vec{d}/2)$. The angle between the vectors is then given by

$$\cos \theta = 1 - \frac{1}{4} [(\vec{\nabla}\alpha \cdot \vec{d})^2 + (\vec{\nabla}\beta \cdot \vec{d})^2 + (\vec{\nabla}\gamma \cdot \vec{d})^2],$$

which is a function of \vec{d} . For every vector \vec{d} there are now

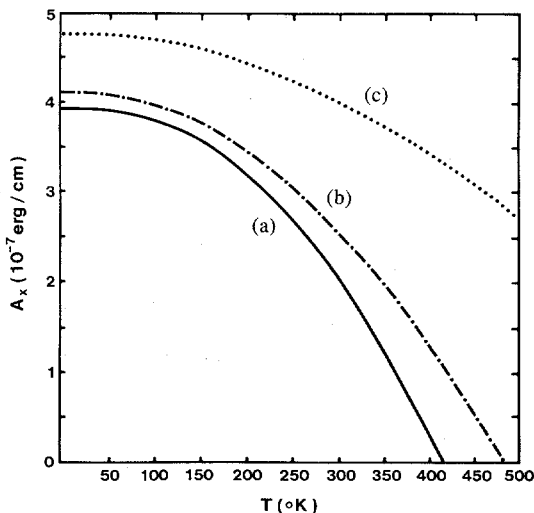


Fig. 12. Calculated exchange stiffness coefficient A_x versus temperature for (a) $(\text{Tb}_{21}\text{Fe}_{79})_{95}\text{Ar}_5$ with $J_{\text{Fe}} = 0.97$ and $\alpha = 0.25$; (b) $(\text{Gd}_{25}\text{Fe}_{75})_{95}\text{Ar}_5$ with $J_{\text{Fe}} = 0.95$, $\alpha = 0.33$; and (c) $(\text{Gd}_{21}\text{Co}_{79})_{95}\text{Ar}_5$ with $J_{\text{Co}} = 0.63$.

two other vectors, \vec{d}' and \vec{d}'' , such that the three are mutually orthogonal. Then $(\vec{\nabla}\alpha \cdot \vec{d})^2 + (\vec{\nabla}\alpha \cdot \vec{d}')^2 + (\vec{\nabla}\alpha \cdot \vec{d}'')^2 = (\vec{\nabla}\alpha)^2 d^2$. The same is true for β and γ . Consequently, the spatial average of $\cos \theta$ is given by

$$\langle \cos \theta \rangle = 1 - \frac{1}{12} [(\vec{\nabla}\alpha)^2 + (\vec{\nabla}\beta)^2 + (\vec{\nabla}\gamma)^2] d^2.$$

The excess energy above the aligned state is now written as

$$\Delta E = \frac{1}{12} \sum_m \sum_n \mathcal{J}_{mn} \langle j_m \rangle \langle j_n \rangle \cdot d_{mn}^2 [(\vec{\nabla}\alpha)^2 + (\vec{\nabla}\beta)^2 + (\vec{\nabla}\gamma)^2]$$

with m, n being nearest neighbors and d_{mn} the distance between nearest neighbor atoms, which is equal to the sum of atomic radii r_m and r_n . The macroscopic exchange stiffness coefficient A_x is then given by

$$A_x = \frac{1}{12} \sum_{n=1}^3 N x_n \sum_{m=1}^3 Z_n x_m \mathcal{J}_{mn} \langle j_m \rangle \langle j_n \rangle d_{mn}^2. \quad (10)$$

Fig. 12 shows the calculated temperature dependence of A_x for representative compositions from the three groups of alloys studied in Section III. (The selected compositions have compensation points in the vicinity of room temperature.) It is observed that the exchange stiffness coefficient is dominated by the transition metal subnetwork in these alloys. A_x drops with temperature until it reaches zero at the Curie point.

VI. MACROSCOPIC ANISOTROPY ENERGY CONSTANT

There are two basically different sources of anisotropy in amorphous rare earth-transition metal alloys. The first is the pair ordering due to inhomogeneous atomic distribution, whereby the classical dipole-dipole interactions create a distinct axis of anisotropy [19]. The anisotropy energy density of pair ordering may be written as

$$E = - \sum_{n=1}^3 N x_n \langle j_n \rangle \cos \theta \sum_{m=1}^3 D_{mn} Z_n x_m \langle j_m \rangle \cos \theta \quad (11)$$

where D_{mn} is the anisotropy coefficient for nearest neighbor pairs. This coefficient is positive for pairs with parallel moments and negative for pairs with antiparallel moments, assuming that the atoms are already arranged in pairs such that both parallel and antiparallel moments prefer their current positions. From symmetry it must be clear that $D_{mn} = D_{nm}$.

The second source of anisotropy is the interaction of atomic charge distribution with local electric fields [17]. If the charge distribution is nonspherical, the electric fields force the distribution, and consequently the orbital angular momentum, into a preferred orientation, and the spin orients itself accordingly through the spin-orbit coupling. In RE-TM alloys the orbital moment of TM is usually small, making its interaction with electric field insignificant. The non-S state RE ions, however, couple strongly to the field and create random axis anisotropy. To simplify the problem, we have assumed the following expression for the single-ion anisotropy energy density

$$E = -N \sum_{n=1}^3 x_n D_n \langle j_n \rangle^2 \cos^2 \theta. \quad (12)$$

where D_n is the single-ion anisotropy constant. The total macroscopic anisotropy energy constant K_u is thus given by

$$K_u = N \left\{ \sum_{n=1}^3 \sum_{m=1}^3 D_{mn} Z_n x_n x_m \langle j_n \rangle \langle j_m \rangle + \sum_{n=1}^3 D_n x_n \langle j_n \rangle^2 \right\}. \quad (13)$$

D_{mn} and D_n have complicated relations with the structure of the media, but for our purposes it is sufficient to treat them as adjustable parameters.

Fig. 13 shows K_u versus temperature for two GdCo-based alloys. The experimental data, taken from the literature, is in good agreement with model calculations. In both cases, $D_n = 0$ and $D_{mn} = \pm 10^{-19}$, with the plus sign applicable to Co-Co and Gd-Gd pairs, and the minus sign applicable to Gd-Co pairs.

Fig. 14 shows K_u versus atomic percent Gd in GdFe alloys at room temperature. There is a rather large scatter in reported data in this case, as is evident from the figure. We believe that part of this scatter is due to the fact that, near compensation point, the magnetization is small and measurements of K_u are subject to large errors. It is also a well-known fact that preparation conditions such as argon pressure and bias voltage during sputtering affect the anisotropy energy through structural variations. The solid curve is calculated from the available data in the mean-field approximation. The anisotropy parameters used are identical to those of GdCo alloys in Fig. 13, namely $D_n = 0$ and $D_{mn} = \pm 10^{-19}$. The agreement in the order of magnitude between this curve and the experimental data suggests that the anisotropy in GdFe is controlled by pair ordering, and that single-ion anisotropy does not play a major role here. This is in agreement with the fact that Gd^{3+} is an S-state ion.

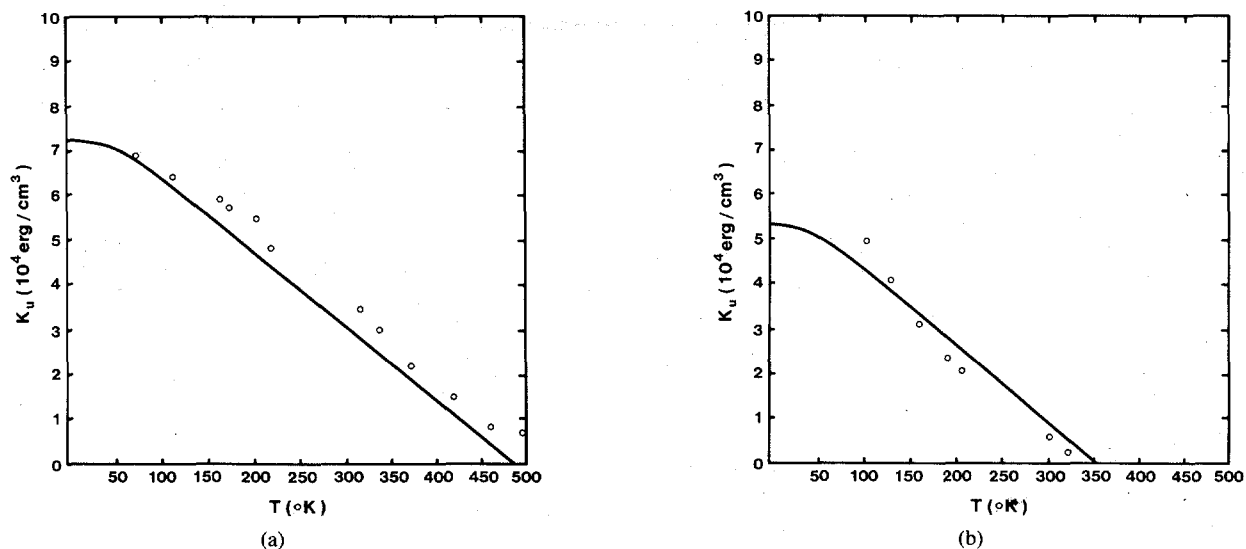


Fig. 13. Macroscopic anisotropy energy constant K_u versus temperature for (a) $\text{Gd}_{15}\text{Co}_{74}\text{Mo}_{11}$ as reported in [21] (solid curve calculated for $(\text{Gd}_{15}\text{Co}_{74}\text{Mo}_{11})_{94}\text{Ar}_6$ with $J_{\text{Co}} = 0.49$), and (b) $\text{Gd}_{11.3}\text{Co}_{67.2}\text{Mo}_{16}\text{Ar}_{5.5}$ as reported in [19] (solid curve calculated for $\text{Gd}_{12.5}\text{Co}_{66.5}\text{Mo}_{16}\text{Ar}_5$ with $J_{\text{Co}} = 0.39$). For both calculations, $D_{mn} = \pm 10^{-19}$ and $D_n = 0$.

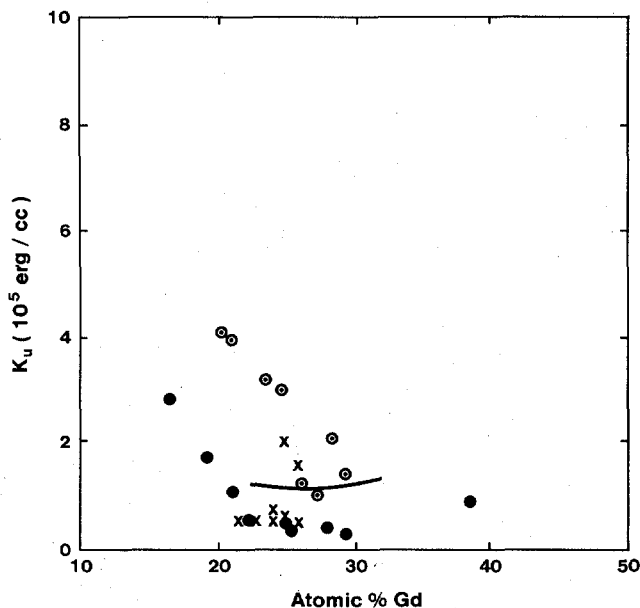


Fig. 14. Macroscopic anisotropy energy constant K_u versus rare earth concentration in GdFe alloys at room temperature. \circ indicates [2], \bullet indicates [24], and \times indicates [25]. The solid line is obtained from available mean-field data with $D_{mn} = \pm 10^{-19}$ and $D_n = 0$.

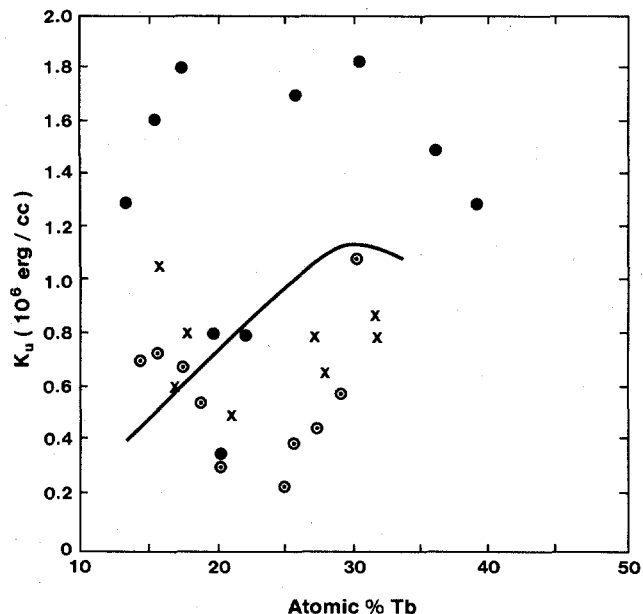


Fig. 15. Macroscopic anisotropy energy constant K_u versus rare earth concentration in TbFe alloys at room temperature. \circ indicates [2], \bullet indicates [24], and \times indicates [3]. The solid line is obtained from available mean-field data with $D_{mn} = \pm 10^{-19}$, $D_1 = 40 \times 10^{-19}$, $D_2 = D_3 = 0$.

Fig. 15 shows K_u versus atomic percent Tb in TbFe alloys at room temperature. The scatter in the experimental data probably arises from the same sources as discussed in the previous case. The solid line is based on available mean-field data and corresponds to $D_{mn} = \pm 10^{-19}$, $D_1 = 40 \times 10^{-19}$, and $D_2 = D_3 = 0$. The explanation is that Tb^{3+} , being a non-S-state ion, is subject to strong axial anisotropy which dominates K_u in TbFe alloys. Notice that D_1 , although much larger than the pair ordering coefficients D_{mn} , is still too small to have significant effect on the mean-field model calculations (see Fig. 11).

VII. CONCLUDING REMARKS

The models developed in this paper can be applied in the analysis of thermomagnetic recording and erasure processes whereby a focused laser beam elevates the local temperature of the recording medium to allow a weak magnetic field to create/annihilate a small magnetic domain. We have reported a preliminary study of this kind in a separate publication [20].

A significant characteristic of the media, connected with the formation and stability of domains in thermomagnetic recording, is the domain wall energy density σ_w . This parameter is related to the exchange stiffness coefficient and

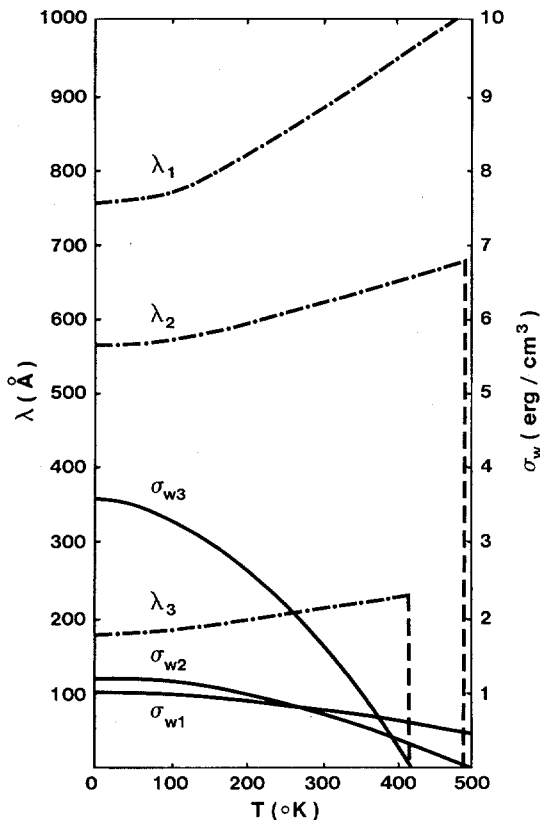


Fig. 16. Calculated domain wall thickness λ and energy density σ_w versus temperature for (1) $(\text{Gd}_{21}\text{Co}_{79})_{95}\text{Ar}_5$, (2) $(\text{Gd}_{25}\text{Fe}_{75})_{95}\text{Ar}_5$, and (3) $(\text{Tb}_{21}\text{Fe}_{79})_{95}\text{Ar}_5$. All compositions have compensation points in the vicinity of room temperature.

the anisotropy energy constant by $\sigma_w = 4\sqrt{A_x K_u}$. Fig. 16 shows the calculated σ_w versus temperature curves for the representatives of the three classes of materials studied in this paper. Also shown are the calculated temperature dependencies of the domain wall thickness $\lambda = 4\sqrt{A_x/K_u}$. (All compositions have room temperature compensation points.) Notice that the TbFe alloy has a larger room temperature σ_w compared with the GdFe and GdCo compounds. This could result in less stable domains for TbFe if it were not for the higher coercivity of this material. On the other hand, the narrower domain wall of TbFe is suitable for high-density recording applications where the domains are densely packed and a large readout signal is required.

In conclusion, we have developed a mean-field model for amorphous RE-TM alloys that can explain the available experimental results with good accuracy. We have postulated the existence of an idealized antiferromagnetic subnetwork for the iron-based alloys and have shown that its presence will result in two different values for the iron moment at nonzero temperatures. In reality, however, our idealized assumption of equal but opposite exchange coefficients for iron ($\pm J_{\text{Fe}-\text{Fe}}$) is not exactly valid. Most probably, there is a distribution of exchange interactions among neighboring iron atoms, with the result that the iron moments will be distributed in a continuous fashion in a certain range. It may be possible to obtain some useful information about the distribution of iron moments

from the Mössbauer spectroscopy. Measurements of the magneto-optic Kerr effect and the extraordinary Hall effect versus temperature, which provide information about the transition metal subnetwork, will also be helpful for the purpose of verification of the model.

We have used our mean-field model to estimate some other properties of the thin film alloys, such as the anisotropy energy constant and the domain wall characteristics. The anisotropy energy constant, in particular, is a function of the deposition environment and the structural characteristics of the films; these dependencies influence the values of our adjustable parameters D_n and D_{mn} . A systematic study of magnetic anisotropy in these films must therefore be undertaken in order to determine the exact nature of this relationship.

REFERENCES

- [1] P. Chaudhari, J. J. Cuomo, and R. J. Gambino, "Amorphous metallic films for magneto-optic applications," *Appl. Phys. Lett.*, vol. 22, pp. 337-339, Apr. 1973.
- [2] Y. Mimura, N. Imamura, T. Kobayashi, A. Okada, and Y. Kushi, "Magnetic properties of amorphous alloy films of Fe with Gd, Tb, Dy, Ho, and Er," *J. Appl. Phys.*, vol. 49, pp. 1208-1215, Mar. 1978.
- [3] T. Chen, D. Cheng, and G. B. Charlan, "An investigation of amorphous Tb-Fe thin films for magneto-optic memory applications," *IEEE Trans. Magn.*, vol. MAG-16, pp. 1194-1196, Sept. 1980.
- [4] Y. Togami, "Magneto-optic disk storage," *IEEE Trans. Magn.*, vol. MAG-18, pp. 1233-1237, Nov. 1982.
- [5] G. A. N. Connell, R. Allen, and M. Mansuripur, "Magneto-optical properties of amorphous terbium-iron alloys," *J. Appl. Phys.*, vol. 53, pp. 7759-7761, Nov. 1982.
- [6] M. Urner-Wille, P. Hansen, and K. Witter, "Magnetic, magneto-optic, and switching properties of amorphous GdFeSn-alloys," *IEEE Trans. Magn.*, vol. MAG-16, pp. 1188-1193, Sep. 1980.
- [7] D. Chen, G. N. Otto, and F. M. Schmit, "MnBi films for magneto-optic recording," *IEEE Trans. Magn.*, vol. MAG-9, pp. 66-83, June 1973.
- [8] E. Bernal G., "Mechanism of Curie-point writing in thin films of MnBi," *J. Appl. Phys.*, vol. 42, pp. 3877-3887, Sep. 1971.
- [9] B. G. Huth, "Calculations of stable domain radii produced by thermomagnetic writing," *IBM J. Res. Dev.*, pp. 100-109, 1974.
- [10] R. Hasegawa, "Temperature and compositional dependence of magnetic bubble properties of amorphous Gd-Co-Mo films," *J. Appl. Phys.*, vol. 46, pp. 5263-5267, Dec. 1975.
- [11] N. Heiman, K. Lee, R. I. Potter, and S. Kirkpatrick, "Modified mean-field model for rare earth-iron amorphous alloys," *J. Appl. Phys.*, vol. 47, pp. 2634-2638, June 1976.
- [12] A. Gangulee and R. J. Kobliska, "Mean-field analysis of the magnetic properties of amorphous transition metal-rare earth alloys," *J. Appl. Phys.*, vol. 49, pp. 4896-4901, Sep. 1978.
- [13] R. C. Taylor and A. Gangulee, "Magnetic properties of amorphous GdFeB and GdCoB alloys," *J. Appl. Phys.*, vol. 53, pp. 2341-2343, Mar. 1982.
- [14] —, "Magnetic properties of the 3d transition metals in the amorphous ternary alloys: $\text{Gd}_{0.2}(\text{Fe}_x\text{Co}_{1-x})_{0.8}$, $\text{Gd}_{0.2}(\text{Co}_x\text{Ni}_{1-x})_{0.8}$, and $\text{Gd}_{0.2}(\text{Fe}_x\text{Ni}_{1-x})_{0.8}$," *Phys. Rev. B*, vol. 22, pp. 1320-1326, Aug. 1980.
- [15] A. Gangulee and R. C. Taylor, "Mean-field analysis of the magnetic properties of vapor deposited amorphous Fe-Gd thin films," *J. Appl. Phys.*, vol. 49, pp. 1762-1764, Mar. 1978.
- [16] C. Kittel, *Introduction to Solid State Physics*. New York: Wiley, 1976, 5th ed.
- [17] M. Cyrot, Ed. *Magnetism of Metals and Alloys*. Amsterdam: N. Holland, 1982.
- [18] E. Callen, Y. J. Liu, and J. R. Cullen, "Initial magnetization, remanence, and coercivity of the random anisotropy amorphous ferromagnet," *Phys. Rev. B*, vol. 16, pp. 263-270, July 1977.
- [19] T. Mizoguchi and G. S. Cargill, "Magnetic anisotropy from dipolar interactions in amorphous ferrimagnetic alloys," *J. Appl. Phys.*, vol. 50, pp. 3570-3582, May 1979.
- [20] M. Mansuripur and G. A. N. Connell, "Energetics of domain for-

- mation in thermomagnetic recording," *J. Appl. Phys.*, vol. 55, pp. 3049-3055, Apr. 1984.
- [21] P. Chaudhari and D. Cronmeyer, "The temperature dependence of the uniaxial anisotropy of $Gd_{1-x-y}Co_xMo_y$ amorphous alloy films on glass substrates," *AIP Conf. Proc.*, vol. 29, pp. 113-114, 1976.
- [22] Y. Mimura, N. Imamura, and T. Kobayashi, "Magnetic properties and Curie point writing in amorphous metallic films," *IEEE Trans. Magn.*, vol. MAG-12, pp. 779-781, Nov. 1976.
- [23] J. J. Rhyne, J. H. Schelleng, and N. C. Koon, "Anomalous magnetization of amorphous $TbFe_2$, $GdFe_2$, and YFe_2 ," *Phys. Rev. B.*, vol. 10, pp. 4672-4679, Dec. 1974.
- [24] H. Takagi, S. Tsunashima, S. Uchiyama, and T. Fujii, "Stress induced anisotropy in amorphous GdFe and TbFe sputtered films," *J. Appl. Phys.*, vol. 50, pp. 1642-1644, Mar. 1979.
- [25] A. Itoh, H. Uekusa, Y. Tarusawa, F. Inoue, and K. Kawanishi, "Magnetostriction and internal stress in GdFe amorphous films with perpendicular anisotropy prepared by rf diode sputtering," *J. Mag. and Mag. Mat.*, vol. 35, pp. 241-242, 1983.
-